The Astrophysical Journal, 602:1024–1036, 2004 February 20

EVIDENCE FOR GRADUAL EXTERNAL RECONNECTION BEFORE EXPLOSIVE ERUPTION OF A SOLAR FILAMENT

Alphonse C. Sterling[1,2] and Ronald L. Moore
NASA/Marshall Space Flight Center, SD50/Space Science Department, Huntsville, AL 35812;
asterling@solar.stanford.edu, ron.moore@nasa.gov
Received 2003 April 28; accepted 2003 September 12

ABSTRACT

We observe a slowly evolving quiet-region solar eruption of 1999 April 18, using extreme-ultraviolet (EUV) images from the EUV Imaging Telescope (EIT) on the *Solar and Heliospheric Observatory* (*SOHO*) and soft X-ray images from the Soft X-ray Telescope (SXT) on *Yohkoh*. Using difference images, in which an early image is subtracted from later images, we examine dimmings and brightenings in the region for evidence of the eruption mechanism. A filament rose slowly at about 1 km s^{-1} for 6 hours before being rapidly ejected at about 16 km s^{-1}, leaving flare brightenings and postflare loops in its wake. Magnetograms from the Michelson Doppler Imager (MDI) on *SOHO* show that the eruption occurred in a large quadrupolar magnetic region with the filament located on the neutral line of the quadrupole's central inner lobe between the inner two of the four polarity domains. In step with the slow rise, subtle EIT dimmings commence and gradually increase over the two polarity domains on one side of the filament, i.e., in some of the loops of one of the two sidelobes of the quadrupole. Concurrently, soft X-ray brightenings gradually increase in both sidelobes. Both of these effects suggest heating in the sidelobe magnetic arcades, which gradually increase over several hours before the fast eruption. Also, during the slow pre-eruption phase, SXT dimmings gradually increase in the feet and legs of the central lobe, indicating expansion of the central-lobe magnetic arcade enveloping the filament. During the rapid ejection, these dimmings rapidly grow in darkness and in area, especially in the ends of the sigmoid field that erupts with the filament, and flare brightenings begin underneath the fast-moving but still low-altitude filament. We consider two models for explaining the eruption: ''breakout,'' which says that reconnection occurs high above the filament prior to eruption, and ''tether cutting,'' which says that the eruption is unleashed by reconnection beneath the filament. The pre-eruption evolution is consistent with gradual breakout that led to (and perhaps caused) the fast eruption. Tether-cutting reconnection below the filament begins early in the rapid ejection, but our data are not complete enough to determine whether this reconnection began early enough to be the cause of the fast-phase onset. Thus, our observations are consistent with gradual breakout reconnection causing the long slow rise of the filament, but allow the cause of the sudden onset of the explosive fast phase to be either a jump in the breakout reconnection rate or the onset of runaway tether-cutting reconnection, or both.

Subject headings: Sun: corona — Sun: flares — Sun: UV radiation

1. INTRODUCTION

Study of coronal behavior during filament eruptions, with a few exceptions (e.g., Kahler, Webb, & Moore 1981, who used *Skylab* data), has had to await the high-cadence space-borne telescopes on board the *Yohkoh* and *Solar and Heliospheric Observatory* (*SOHO*) satellites (e.g., McAllister et al. 1996; Innes et al. 1999; Schmieder et al. 2000; Zhang & Wang 2001). As is apparent from those and other studies, flares and filament eruptions are different aspects of a general magnetic eruption process, with a standard reconnection flare model having evolved to explain several eruption features (e.g., Hirayama 1974; Forbes 1990; Shibata et al. 1995). In that model, the flare heating is driven by reconnection in the wake of the eruption of the magnetic field that threads and carries the filament. Just what initiates and drives the filament-field eruption itself, however, remains unsettled and controversial.

In a preliminary study, Sterling, Moore, & Thompson (2001b) used *Yohkoh* and *SOHO* coronal data of a filament eruption to address the question of the cause of the eruption onset. They found that upward acceleration of the filament began prior to or concurrent with the start of extreme-ultraviolet (EUV) flare brightening under the erupting filament. In one version of the standard model, known as the ''tether cutting'' model (e.g., Moore & LaBonte 1980; Sturrock 1989; Moore & Roumeliotis 1992; Moore et al. 2001), reconnection among highly sheared magnetic fields below a filament (or low in a filament channel) initiates and releases the eruption. Sterling et al. (2001a), however, suggested that while tether cutting may have been important after the eruption was underway, it did not start the eruption in that event.

In this paper, we examine in greater detail the same event as Sterling et al. (2001b) in an attempt to learn more about the eruption-onset mechanism, including the possible role of tether cutting in driving the eruption. Although that eruption occurred in a quiet region and produced only a weak flare, an advantage is that the evolution to eruption was relatively slow, allowing for closer scrutiny than generally possible for active region eruptions, which usually evolve more quickly. Unlike our earlier study, here we will use difference images (in which an earlier image is subtracted from later images) to look for locations of intensity dimmings and brightenings over time. In at least some cases, locations where dimmings occur, referred

[1] United Applied Technologies, Inc., 11506 Gilleland Drive, Huntsville, AL 35803.
[2] Current Address: Institute of Space and Astronautical Science, Yoshinodai 3-1-1, Sagamihara, Kanagawa 229-8510, Japan.

to as "dimming regions," are likely caused by a density reduction due to the outflow of material (e.g., Zarro et al. 1999; Gopalswamy & Thompson 2000; Harra & Sterling 2001). In other cases, dimmings could happen because material either cools or heats until it no longer emits in the passband being used to make the observations. We look at the relative timings of dimming onsets in our event and compare them with the onsets of other pre-eruption and early-eruption signatures. With this information, along with combined imaging and magnetic data, we consider which theoretical mechanisms are or are not consistent with our observations.

As in other of our recent works (Sterling & Moore 2001a, 2001b; Sterling et al. 2001a), we will focus our theoretical considerations on two specific ideas: the tether-cutting model mentioned above and the "breakout model" put forth by Antiochos (1998) and Antiochos, DeVore, & Klimchuk (1999). These models differ in that tether cutting requires only a single-bipole magnetic field and has the initial reconnection in the sheared-field core of the bipole, while breakout requires a multipolar magnetic field and has the initial reconnection at a neutral point far removed from the core field that explodes in the eruption. Although we do not consider other suggested mechanisms in detail, we present our data and analysis results without reference to any particular model until § 4, so that readers may apply our observational results, derived in § 2 and § 3, to any model they wish to consider.

2. INSTRUMENTATION AND DATA

For our study we use imaging data in EUV and soft X-rays, supplemented with line-of-sight magnetograms. Our EUV data are from EIT on *SOHO*, which takes full-disk images in four EUV filters and uses a CCD detector with 2.″6 pixels. We primarily use data from the 195 Å Fe XII filter, images that are generally taken with a cadence of about 12 minutes; this filter has its greatest sensitivity to coronal plasmas at 1.5 MK. We also use EIT data taken with the 304 Å filter, which observes emission of both He II from plasma at 2×10^4 to 8×10^4 K and of Si XI from plasma at 1 MK. *SOHO* is in a solar orbit at the L1 Lagrange point and therefore is not subject to spacecraft night. Delaboudiniere et al. (1995) give a description of EIT.

Our soft X-ray data are from SXT on *Yohkoh*. SXT observes the approximate range of 3–45 Å in several filters and can take either full-disk or partial-disk solar images. For this study we restrict our analysis to the full-disk images, which have effective pixel resolution of either 4.″9 or 9.″8; none of the 4.″9 resolution images are from the pre-eruption phase, however. Our data are from the AlMg filter, which is most sensitive to coronal emissions in excess of approximately 2–3 MK. Time cadence for the images vary, with typical values of about 8–10 minutes and occasional larger gaps. *Yohkoh* also undergoes a day-night cycle, causing regular disruption to continuity of the images. Tsuneta et al. (1991) give full SXT instrumental details.

We also use 2.″0-pixel magnetograms from *SOHO*'s MDI instrument (Scherrer et al. 1995) for magnetic field data.

As Sterling et al. (2001b) describe, this eruption occurred on 1999 April 18 with the soft X-ray intensity increase starting in SXT images between 06:33 UT and 07:21 UT. In EUV, the filament was stationary or oscillating in place until about 00:00 UT on 1999 April 18. It then showed pre-eruption upward movement between 00:00 UT and 06:36 UT on 1999 April 18 with an approximate velocity projected against the solar disk of 1.2 km s^{-1}. Between EIT images at 06:36 UT and 06:48 UT, the filament abruptly accelerated and began the fast phase of its eruption; between 06:36 UT and 07:25 UT, its average upward velocity was 16.5 km s^{-1} (Figs. 1*a* and 7, below). Although the eruption did not produce a *GOES* X-ray flux above mid-B class, it did produce postflare loops in both EUV and soft X-rays, indicating that it was similar to standard two-ribbon flares. LASCO, the coronagraphs on *SOHO*, detected at about 08:30 UT on the same date a partial halo coronal mass ejection (CME), which was likely from this eruption.

3. OBSERVATIONS

3.1. *Overall Morphology*

Figures 1, 2, and 3 show the general morphology of the erupting region in EIT 195 Å, SXT, and EIT 304 Å images, respectively. For each figure, the top three panels show images at various times, and the bottom three images show difference images with an appropriate pre-eruption image subtracted from the respective image in the panel immediately above.

In the EIT 195 Å images, comparing Figures 1*a* and 1*b* reveals the filament's pre-eruption upward movement relative to the bright point at approximately (−200″, 600″). Figure 1*b* shows the filament erupting, and, by the time of Figure 1*c*, the filament is gone and post-flare loops cover part of the region where it once existed.

Figures 1*d*–1*f* show the development of dimming regions in EIT 195 Å, relative to an image just after the start of the filament's pre-eruption slow upward movement. Figure 1*e* shows dimming regions developing on either side of the filament's original location; that to the northwest side is between (0″, 550″) and (200″, 350″) and that to the southeast side is between (−200″, 500″) and (−50″, 400″). Images between those of Figures 1*e* and 1*f* show that the two regions grow and progressively become darker between the two figures. Postflare loops develop out of the central portion and cover portions of both dimming regions by the time of Figure 1*f*. Only the ends of the filament fields, which (before the eruption) bulge out from beneath an overlying restraining arcade of field, leave a persistent dimming pattern, since the stretched legs of this arcade reconnect in the wake of the eruption to form the postflare loops, which eventually replace much of the dimming. Moore et al. (2001) refer to these bulging fields as "elbows," and the locations vacated by these elbows when the filament erupts result in a pattern of "double dimmings." Such double dimmings have been seen in association with soft X-ray sigmoids in active regions (Sterling & Hudson 1997; Hudson et al. 1998).

Figure 2 shows soft X-ray images from SXT with the pre-eruption (Figs. 2*a* and 2*d*) and the post-eruption (Figs. 2*c* and 2*f*) situations similar to the corresponding EIT images in Figure 1 (Figs. 1*a* and 1*d*, and Figs. 1*c* and 1*f*, respectively). Figure 2*a* shows that there is virtually no enhanced soft X-ray emission in the filament region prior to eruption. Flare loops begin in the central portion of the filament channel in Figure 2*b* and spread the length of the channel in Figure 2*c*. In the EIT 195 Å image closest in time (07:48 UT) to Figure 2*b*, the filament is no longer visible and postflare loops are beginning to extend from the eruption center in both directions along the filament channel. (Fig. 8*b* shows an SXT image at 07:21, near the time of the 07:25 UT [Fig. 1*b*] EIT 195 Å image.)

In the soft X-ray difference images, many of the dimmings and brightenings already apparent in Figure 2*d* and continuing in the other two difference image panels are not associated with the eruption. Rather, they are spurious, resulting from jitter due to spacecraft motion or image processing, and can be as large as

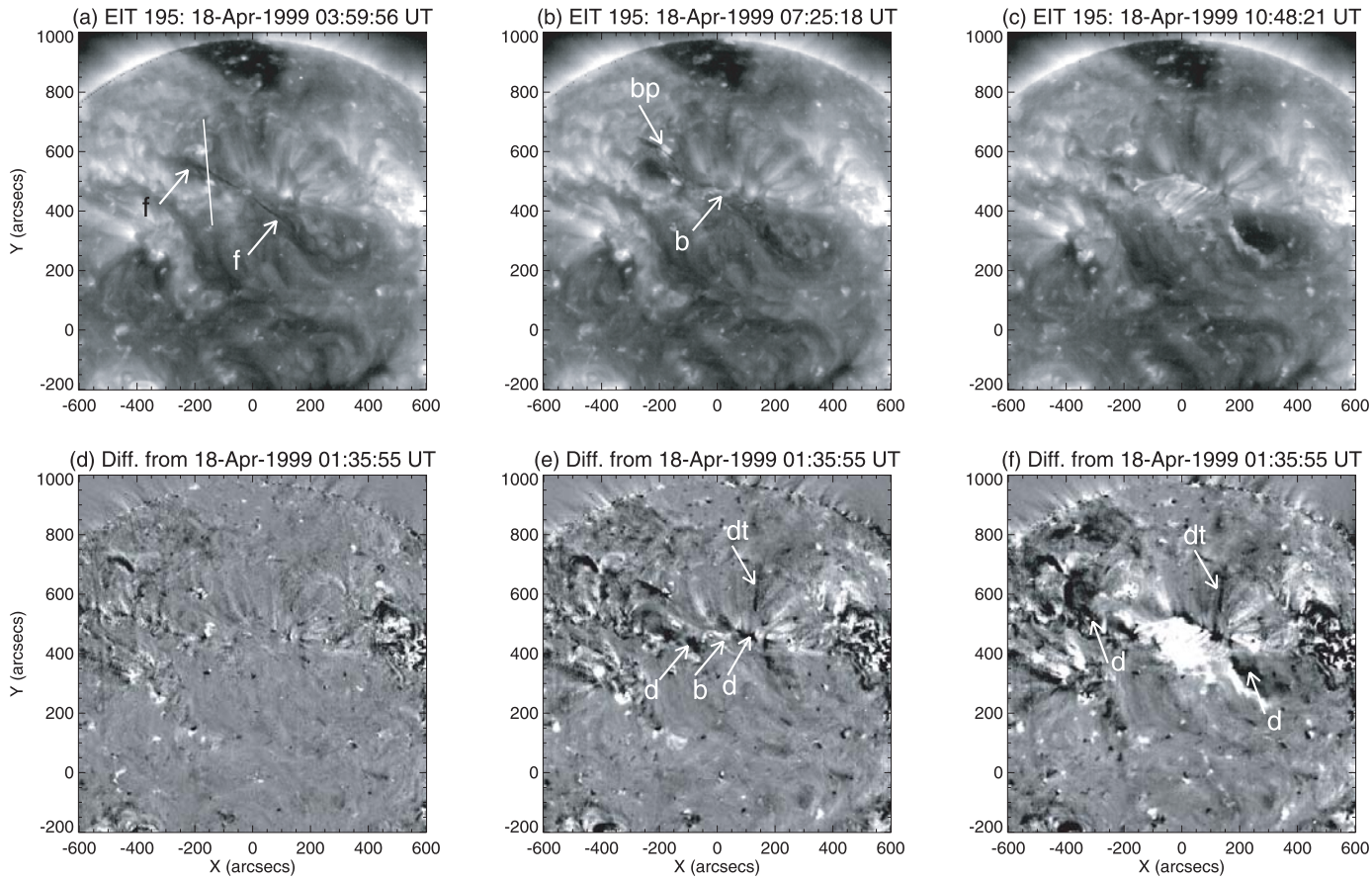

FIG. 1.—EIT 195 Å images of the quiet-region filament eruption. (*a*) and (*b*). Prior to the eruption, the filament moves upward between the times of these two images. The thin, nearly vertical line in (*a*) is a fiducial used to measure the projected rise of the filament over time (shown in Fig. 7*a*), and only part of the erupting filament is still visible in (*b*). (*c*) Post-flare loops are visible in the region following eruption. Panels *d*–*f* show difference images, formed by subtracting a 1999 April 18 01:35:55 UT image from the images in (*a*)–(*c*), respectively. Arrows labeled "f" in (*a*) point to the filament. The arrow labeled "bp" in (*b*) points to a bright point that a part of the filament is crossing in this image and relative to which the filament has moved since (*a*). Arrows labeled "b" in (*b*) and (*e*) indicate brightenings due to very young flare ribbons developing in the magnetic core region. Arrows labeled "d" in (*e*) and (*f*) point to locations of dimmings associated with the filament eruption that we believe are associated with mass expulsion, where those arrows in (*f*) indicate the "double dimmings" discussed in the text. Arrows labeled "dt" in (*e*) and (*f*) point to a region of dimming that we believe is due to a temperature change rather than a mass expulsion. East is left and north is toward the top in this and all other figures.

about 20″ in some of these SXT frames. Other intensity variations with time occur because of changes in the solar corona that are not directly involved with the eruption. Faint dimmings near the center portion of Figure 2*d*, however, are real and represent the earliest eruption-associated soft X-ray dimmings. These dimmings occur along the sides of the filament channel with two running largely parallel with a separation of about 100″. They correspond to the EIT 195 Å dimmings discussed above (Fig. 1*e*); those EIT dimmings, however, did not become detectable until near eruption time. These pre-eruption soft X-ray dimmings increase with time in prominence and are clearly visible by 06:00 UT (Fig. 6*c*, discussed below), at least 36 minutes prior to the rapid upward acceleration of the filament. At the times of these pre-eruption dimmings, there is no persistent brightening above noise level at the location where the post-flare loops eventually develop in between the parallel dimmings. Dimmings at this location are consistent with the field arcade straddling the filament expanding upward; the increased volume of the fields would mean a reduced density, resulting in a lower intensity in soft X-rays.

Figure 2*e* shows these same dimmings surrounding the (overexposed) developing post-flare loops. By the time of Figure 2*f*, dimming has developed at the locations indicated by arrows, overlapping the strong elbow dimming in EIT 195 Å in Figures 1*c* and 1*f*.

Figures 3*a*–3*c* show the eruption region in EIT 304 Å images, with the first two panels near the times of the corresponding images in Figures 1 and 2. While Figure 3*c* is somewhat later than the corresponding images in Figures 1 and 2, it is the closest in time following the eruption available in 304 Å. Figure 3*b* shows the filament just starting to erupt, while most or all of it has disappeared in Figure 3*c*. Figure 3*b* (at 07:19 UT) shows that two flare ribbons, one on each side of the filament, brightened early in the fast phase of the eruption, while the filament was still near its initial position. These flare ribbons are at the feet of the young flare arcade seen in the SXT image in Figure 8*b* 2 minutes later (at 7:21 UT).

Although the corresponding difference images in Figures 3*d*–3*f* are noisy, they appear to show development of dimming regions near, for example, the locations indicated by arrows in Figure 3f; these correspond to the locations of the double dimmings discussed in connection with the EIT 195 Å images.

3.2. *False Dimmings and Brightenings*

Before further analyzing the true dimmings in the EIT and SXT images, we consider the magnitude of spurious dimmings

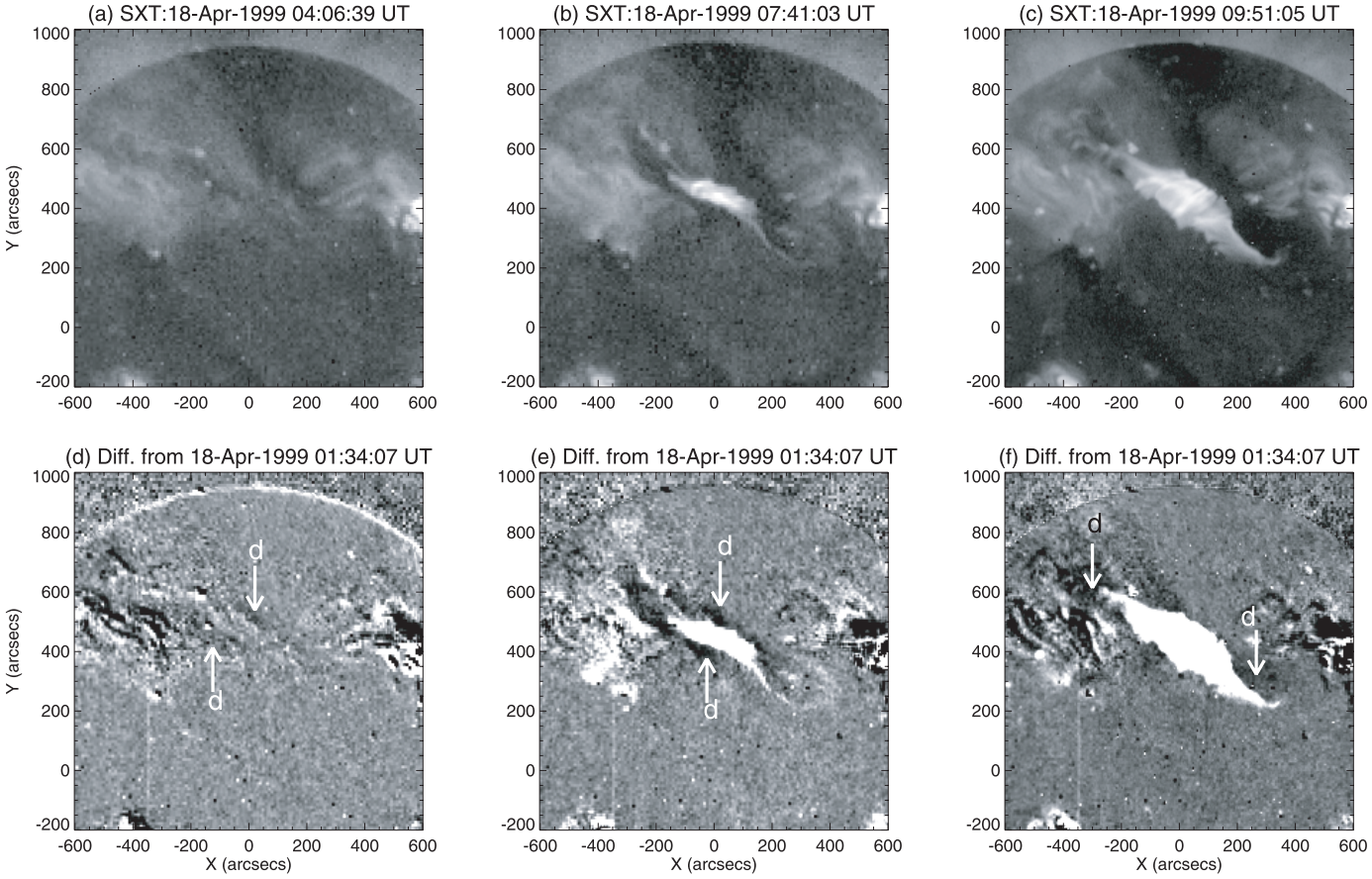

FIG. 2.—Similar to Fig. 1, but for SXT images taken with the AlMg filter. Panels *a–c* are at similar times to images in Fig. 1 (*a*)–(*c*), although the filament moved significantly between the times of Fig. 1*b* and 2*b*. Panels *d–f* show difference images formed by subtracting an image from 1999 April 18 01:34:07 UT from the images in (*a*)–(*c*), respectively. Arrows in (*d*) point to dimming regions developing on either side of the filament during the pre-eruption phase, and arrows in (*e*) point to dimmings near the same locations just after eruption onset. Double dimmings are fainter than those in Fe XII, but they are visible in (*f*) near locations indicated by the arrows.

resulting from systematic factors. This is important for our current work, since we extend the time between differenced images to several hours.

Figure 4 shows full-disk images from EIT and SXT for near the maximum time difference we consider. In addition to dimmings and brightenings associated with the event of this paper in the north, along with other true solar activity, the EIT image shows a tendency toward dimming on the east side and brightening on the west side; the SXT image shows the same effect, but less pronounced. This effect is spurious; we show that it results from a combination of limb brightening in the EUV and soft X-ray images and the corrections we make for solar rotation.

Figure 5 shows light curves of the intensities in the original (i.e. nondifferenced) images at the rotationally shifted locations of the five boxes shown at their initial position in the two Figure 4 images; each of the curves is an integrated average over the area of the respective box. Four of these boxes are on the equator, while the box on the east (left) limb is displaced because of significant solar activity occurring near the east limb equator during the time period we consider. This positioning should not affect our investigations qualitatively, however, since the key factor in this dimming seems to be proximity to the limb more than the latitude.

Figure 5*a* shows the light curves for the EIT 195 Å images. Vertical offsets at the initial time between the curves originating from different longitudes are a consequence of the limb brightening, with boxes nearer the limb having higher initial intensities. This limb brightening is a well-known effect due to the increased atmospheric path length near the limb compared to the disk center; for optically thin lines like Fe XII 195 Å, this results in increased emission in EUV toward the limb, since the total intensity is an integral over the line-of-sight path length. While the light curves from the box near central meridian (box 3) are relatively constant, the light curves from the east side (boxes 1 and 2) both decrease with time, while those from the west side (boxes 4 and 5) increase with time. Nonuniformities in the light curves largely result from brightening and dimming from solar activity, but the overall trends are spurious, having the following explanation in terms of rotation and limb brightening.

Before subtracting a later image from an earlier (reference) image, we differentially rotate both images to a common time; in this study, we chose to rotate all images to 1999 April 18, 11:00:00 UT. Consider the effect of this on a portion of the solar surface that remains quiet during the entire time period, for example, at the location of the east-limb box, box 1. For the first difference image, both the later image and the reference image will be rotated nearly the same amount and, therefore, the difference at box 1 will be about zero; that is, there will be practically no dimming at that location in the difference image for the first small time step. After a few images,

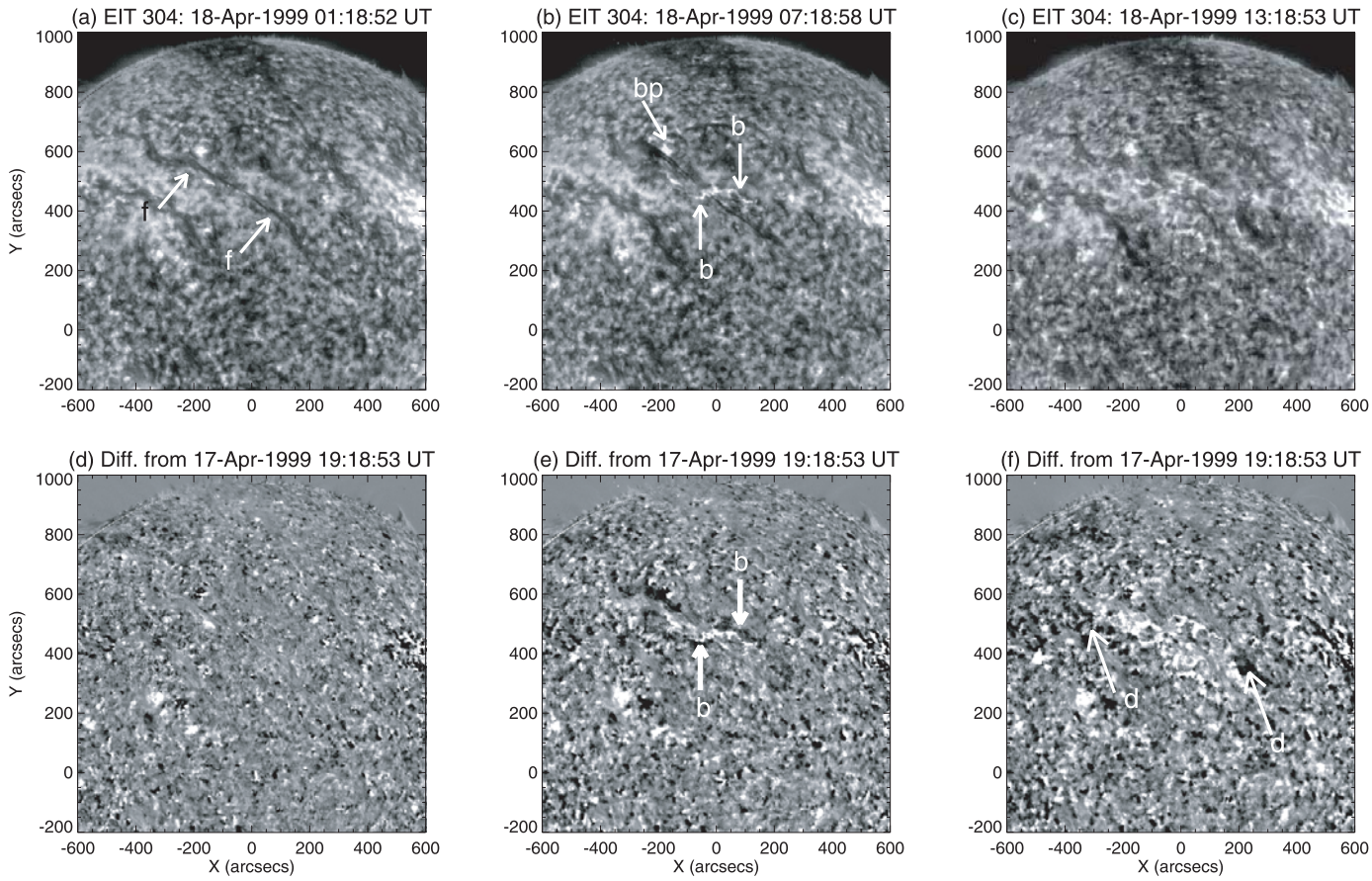

FIG. 3.—Similar to Figs. 1 and 2, but for EIT 304 Å images. Panels *d–f* are difference images formed by subtracting an image at 1999 April 17 19:18:53 UT from the images in (*a*)–(*c*), respectively. Arrows labeled "f" in (*a*) point to the filament. Arrows labeled "b" in (*b*) and (*e*) point to brightenings due to very young flare ribbons developing in the magnetic core region, while the arrow labeled "bp" in (*b*) points to the bright point indicated in Fig. 1*b*; part of the filament is crossing the lower part of this bright point in (*b*). Arrows labeled "d" in (*f*) point to likely double-dimming regions.

however, the box 1 location in the later image will have been rotated by a substantial amount; because of the solar rotation direction, this location will be west of and, therefore, closer to disk center than the corresponding point in the reference image. Because of limb brightening, this closer-to-disk-center location will have lower intensity than the corresponding location in the reference image. Thus, when the reference image is subtracted, that location will have a negative value, and the box 1 location will be dimmed in the overall difference image. Similarly, a location near the west limb will show brightening. We do not state a quantitative value for these false intensity changes, since we do not know how they would differ with factors such as the intensity of the corona in the images.

Figure 5*b* shows that the situation is not as severe in SXT, but it does exist. Overall, however, the SXT data show much more variation than do the EIT images; largest of these is a cyclical orbit-dependent variation in intensity of magnitude ~10%, and this dominates the systematic trends due to the limb brightening for difference images of time spans up to several hours.

These false dimmings and brightenings occur in our "fixed frame" difference images, in which the same initial image is removed from every image for a given wavelength. For images taken at sufficient cadence (such are our EIT 195 Å images), this effect would not be appreciable in "running difference" images in which the image from the previous time step is always subtracted from a given image and the time step is so short that there is negligible rotation.

3.3. *Time Dependence of Eruption-Associated Dimmings and Brightenings*

We now consider the time histories of physically meaningful dimmings and brightenings seen in the difference images. We define two time periods for the dimmings and brightenings based on whether they begin before or during the fast phase of the filament eruption; we call these, respectively, *pre-eruption* or *eruption* dimmings and brightenings.

Figure 6 shows selected difference images: Figures 6*a* and 6*b* are, respectively, posteruption EIT 195 Å and 304 Å images differenced with corresponding pre-eruption images; Figure 6*c*, from SXT, is a difference between two pre-eruption images, one several hours before eruption subtracted from one about 40 minutes before eruption; and Figure 6*d*, also from SXT, is a difference between a posteruption image and the image from several hours before eruption. On each difference image we overlay boxes that we use to define intensity light curves. We selected boxes 1–6 based on features in Figure 6*a*: boxes 1 – 4 are in various dimming (1, 2, and 4) or brightening (3) regions, box 5 covers the region where flare brightening begins, and box 6 covers a region that shows relatively little variation in EIT 195 Å that we take to approximate the EIT 195 Å background. Boxes 7 and 8 are regions with little variation in EIT 195 Å, but that show brightenings in SXT prior to eruption (Fig. 6c).

Figure 7*a* shows the variation with time of the intensity integrated over boxes 1–6 in Figure 6 and derived from the

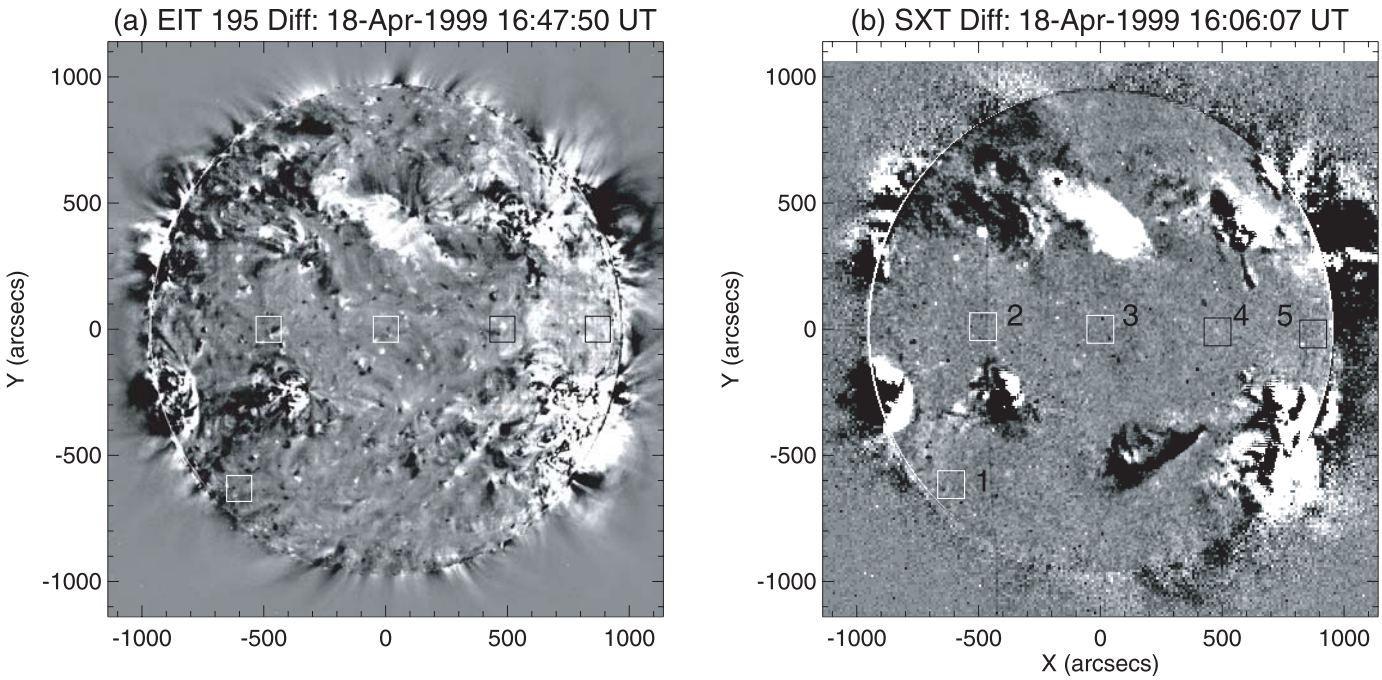

FIG. 4.—(*a*) is an EIT 195 Å difference image with an image at 1999 April 18 01:35:55 subtracted from the image at the time in the label. In addition to the intensity variations apparent around the erupting region of this paper (cf. Fig. 1*f*) and other true solar activity, there is a systematic dimming on the east side (*left*) and brightening on the west side (*right*) due to a combination of EUV limb brightening and rotation between the times of the difference. (*b*) Same as (*a*), but for SXT AlMg, with a 1999 April 18 01:34:07 image subtracted from the image of the time given in the label. For both images, overlaid boxes are regions from which the light curves in Fig. 5 are derived.

original (nondifferenced) images in EIT 195 Å. Figure 7*a* also shows the projected height of the filament along the fiducial of Figure 1*a* as a function of time. Figure 7*b* shows similar intensity variations from the nondifferenced SXT images; we omit light curves for boxes 2 and 6 from Figure 7*b* because the SXT intensities from those boxes are near the background noise level.

Box 1 marks one of the elbow double dimmings discussed earlier; this dimming appears in each of the three wavelengths (e.g., Figs. 6*a*, 6*b*, and 6*d*). Its counterpart near coordinate $(-200'', 500'')$ is also weakly apparent in all three wavelengths (e.g., Figs. 1*f*, 2*f*, and maybe 3*e*). Figure 7*a* shows that the onset at this location of strong dimming in EIT 195 Å occurs nearly simultaneously with the rise in intensity of the flare loops and

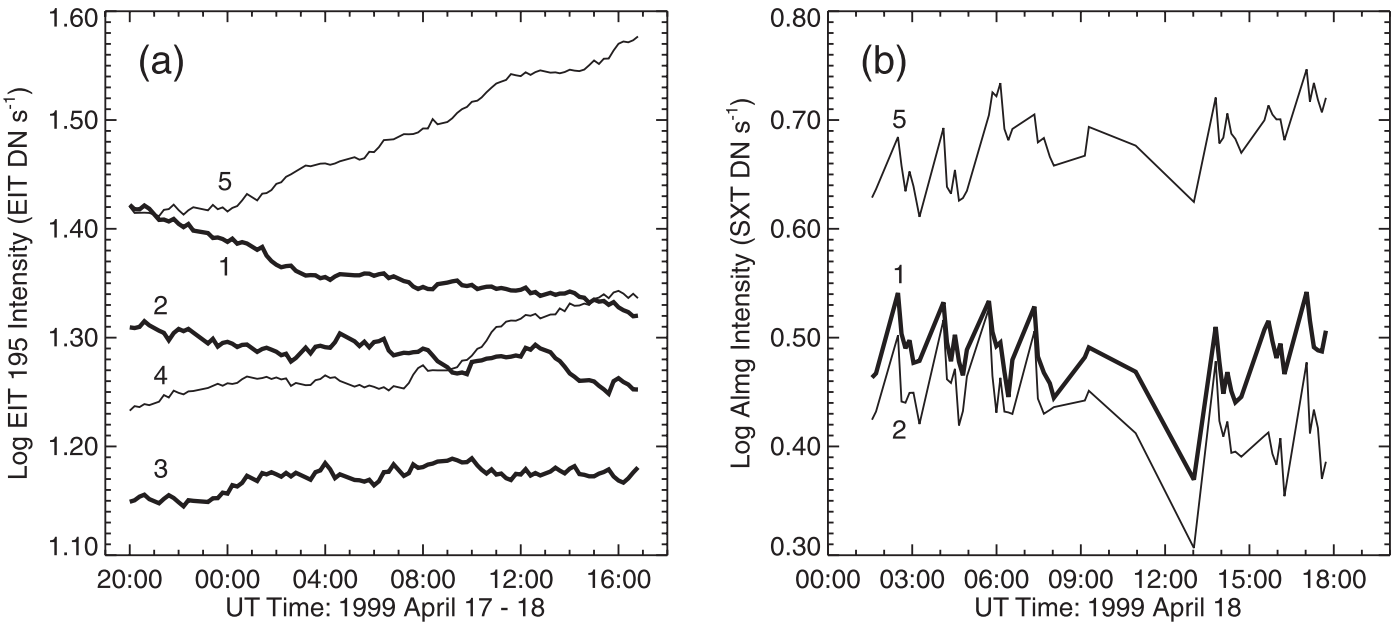

FIG. 5.—Light curves from rotated, nondifferenced images as functions of time for the intensities at the locations of the boxes overlaid on the images in Fig. 4 for (*a*) EIT 195 Å and (*b*) SXT AlMg, in which the intensities are summed and spatially averaged over the box in each case. Light curves for boxes 3 and 4 are omitted from (*b*) for clarity. Lines are plotted with two different thicknesses for clarity. DN (Data Number) units for intensities are defined for SXT and EIT in Tsuneta et al. (1991) and Delaboudiniere et al. (1995), respectively.

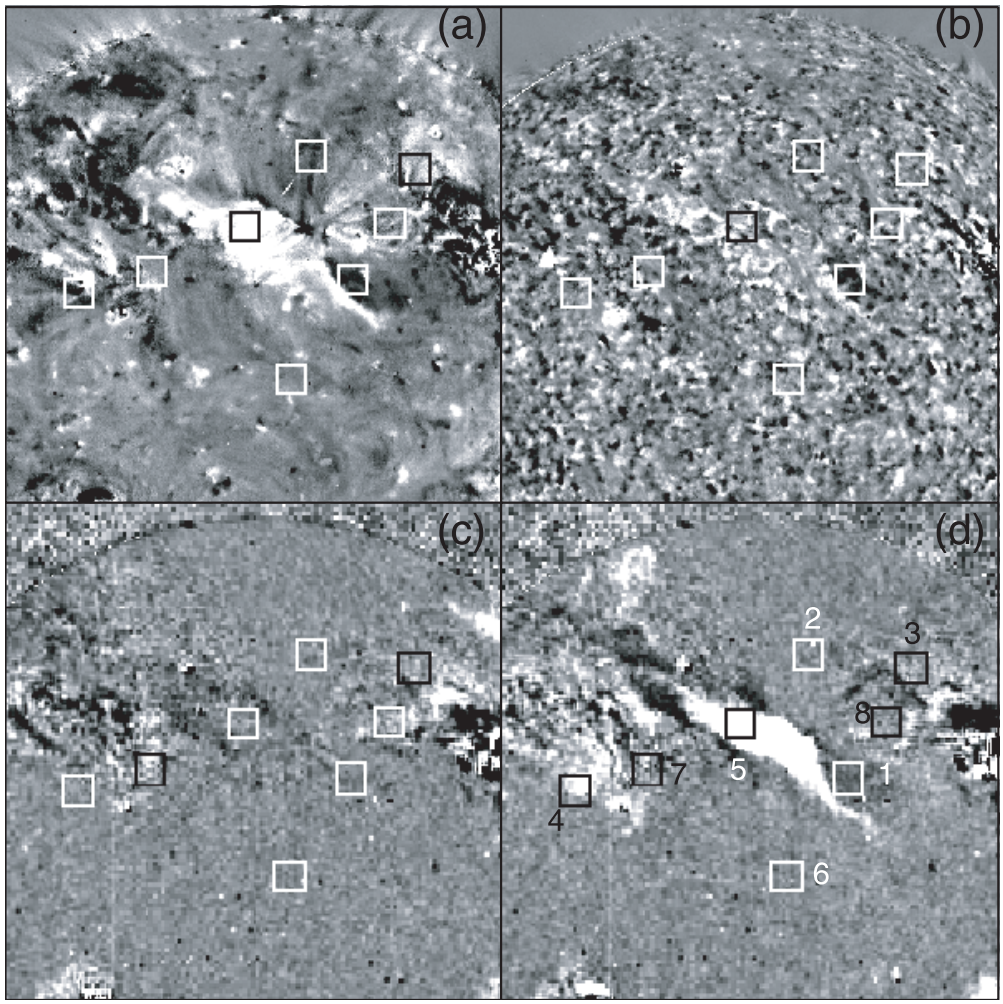

FIG. 6.—Difference images in three different wavelength bands: (*a*) EIT 195 Å with a 1999 April 18 01:35:55 UT image subtracted from a 1999 April 18 12:12:02 UT image; (*b*) EIT 304 Å with a 1999 April 17 19:18:53 UT image subtracted from a 1999 April 18 13:18:53 UT image; (*c*) SXT AlMg with a 1999 April 18 01:34:07 UT image subtracted from a 1999 April 18 05:59:44 UT image; and (*d*) SXT AlMg with a 1999 April 18 01:34:07 UT image subtracted from a 1999 April 18 08:02:23 UT image. Respective boxes indicate identical locations on the Sun in each panel and are used for creating the light curves of Fig. 7 with each box identified by the numbers in panel *d*; boxes are either white or black to improve visibility as needed.

the start of the filament's upward acceleration; therefore, this is an *eruption dimming.* Zarro et al. (1999) also found that dimmings and flare brightenings begin nearly simultaneously in EUV; for their case also, the dimming regions were at locations associated with the elbows of a sigmoid, as discussed by Sterling & Hudson (1997). Figure 7*b* shows that strong dimmings also occur in soft X-rays in the box 1 region after the start of the fast phase of the filament eruption.

Box 2 of Figure 6*a* resides in a region of a more subtle EIT 195 Å dimming. That dimming extends north of the erupting region, and its southern boundary is rooted near the eruption region. It appears in Figures 1*e*, 1*f* and 6*a* and can even be weakly detected as early as Figure 1*d*; thus, this region clearly dims prior to filament eruption. Figure 7*a* indicates that the region shows a slight intensity rise at the start of our observation period, but then begins to fall between 00:00 UT and 01:00 UT; that is, the dimming onset roughly coincides with the start of the filament's rise, and so it is a *pre-eruption dimming.* This dimming ends with the intensity flattening out at about the time of the filament eruption. Thus this region shows dimming that is roughly correlated with the motion of the erupting filament with an intensity drop of ≈30% between 00:00 UT and 06:30 UT. SXT images do not show substantial intensity changes in this region above their noise level, and lack of this corresponding SXT dimming may indicate that the EIT dimming results from heating or cooling of a feature at this location, rather than expulsion of coronal material.

As this dimming is both subtle in EIT and absent in SXT, we seek assurances that it is not spurious. From § 3.2, we understand that the primary systematic spurious dimmings occur east of the central meridian, but this dimming is just west of central meridian; moreover, this dimming is prominent in the full-Sun image of Figure 4*a*. These points give us confidence that it is a real feature.

Box 3 is in a region that shows some brightening in EIT 195 Å images, perhaps beginning prior to filament eruption. These brightenings are weak and may suffer some spurious brightenings from the region's location toward the west limb (§ 3.2). We discuss this region more in § 4.

Box 4 marks a region with both dimmings and brightenings in EIT 195 Å where the dimmings become pronounced nearly in synchronization with those of box 1. Figure 7*b* shows brightenings here in SXT starting at about the same time as the EIT 195 Å dimmings.

Boxes 7 and 8 indicate regions that show subtle brightenings in SXT in Figures 6*c* and 2*e*. Figure 7*b* shows that these

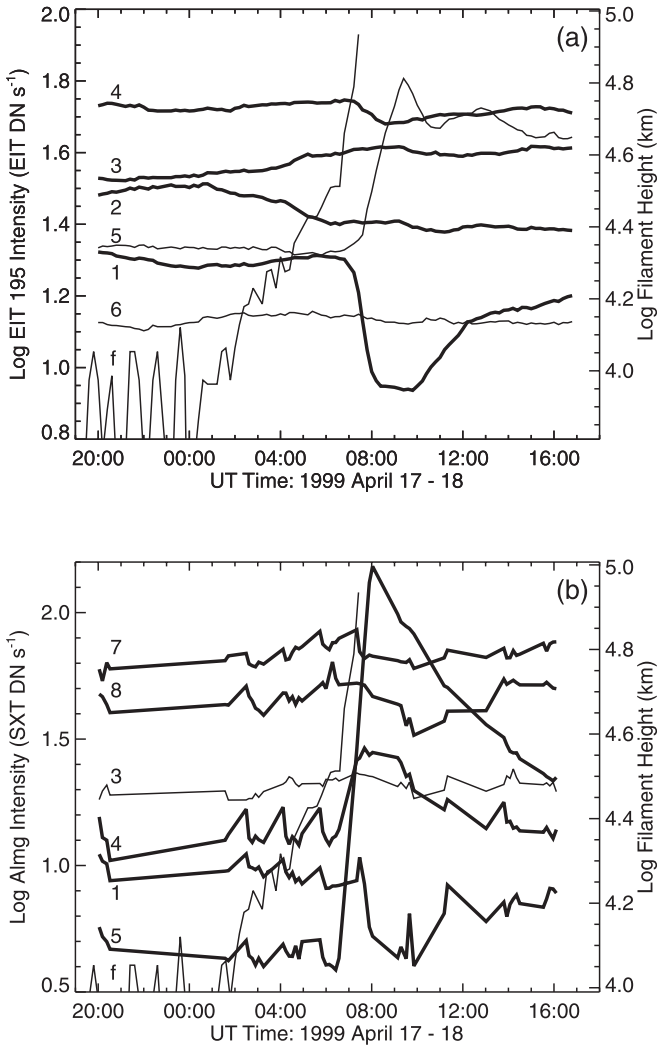

FIG. 7.—(*a*) Light curves from EIT 195 Å images for the boxed regions in Fig. 6*a*, where labels 1–6 identify the boxes correspondingly labeled in Fig. 6*d*. To improve clarity, values for box 3 are shifted by −0.1 on the vertical log scale and curves 7 and 8 are omitted. The curve labeled "f" shows the projected distance the filament moves along the fiducial in Fig. 1*a*; zero height is approximately 5000 km, consistent with the zero location used in Fig. 2 of Sterling et al. (2001a). (*b*) As in (*a*), but light curves from SXT AlMg images (*thick*) with the filament trajectory from (*a*) overlaid. Light curves have been shifted on the vertical log scale to improve clarity as follows: curve 1, −0.1; curve 3, not shifted; curve 4, −0.1; curve 5, −0.6; curve 7, +0.3; curve 8, +0.3. Curves 2 and 6 are omitted for clarity. For both (*a*) and (*b*), random uncertainties in the light curves are comparable to the size of their local fluctuations, and curves are plotted with two different thicknesses for clarity.

brightenings commence prior to the eruption of the filament and the start of the flare brightenings; although the light curves in Figure 7 are noisy, inspection of movies made from the difference images supports this indication. In contrast, EIT 195 Å images show no substantial intensity changes over the period of our observations in Figure 7; we omit these box 7 and 8 light curves from Figure 7*a* for clarity, but their log values cover the ranges 1.13 to 1.17 and 0.56 to 0.64 EIT DN s^{-1}, respectively.

3.4. *Relationship to Magnetic Field*

Figure 8 shows the erupting region's relationship to the magnetic field. Overall, there is a quadrupolar field pattern with alternating positive, negative, positive, and negative regions; we refer to these as magnetic regions 1–4, respectively, as labeled in Figure 8*b*. As expected, the filament overlies a neutral line, the one between magnetic regions 2 and 3. Figures 8*d* and 8*e* show that the regions of dimming running parallel to the filament channel reside in the enhanced fields of magnetic regions 2 and 3. Similarly, one end (the southern end) of the dimming region of box 2 in Figure 6 is rooted in the strong fields running parallel to the filament channel, magnetic region 3. It is likely that at least some of the opposite end of this dimming region connects to magnetic region 4, i.e., that this dimming is in loops connecting magnetic regions 3 and 4. Dimming of box 4 in Figure 6*a* occurs at the edge of magnetic region 1, and the dimmings and brightenings just northwest of box 4 are located in the strongest portion of magnetic region 1. Intensity enhancements in SXT associated with box 7 of Figure 6 occur between magnetic regions 1 and 2 (Fig. 8*e*), indicating that these are in the magnetic loop system connecting magnetic regions 1 and 2; this loop system is discernible in the EIT and SXT images in Figures 1 and 2. Box 3 is in the west side of magnetic region 4 in the feet and legs of the magnetic arcade connecting magnetic regions 3 and 4.

4. DISCUSSION

In summary, we have observed a slowly developing quiet region filament eruption of 1999 April 18 using EUV and soft X-ray images and magnetic field data. For over 6 hours, the filament rises with a velocity of about 1 km s^{-1}, after which it undergoes rapid upward acceleration (its eruption), leaving a weak flare and post-flare loops in the vacated filament channel. We categorized intensity dimmings and brightenings at various locations in difference images as pre-eruption or eruption features, depending on when they started relative to the time of rapid filament ejection onset. We found pre-eruption dimmings in both EUV and soft X-rays during the slow rise of the filament. This event occurred in a quadrupolar magnetic configuration, and comparisons with the magnetograms show the locations of the dimmings and brightenings within this magnetic field. A pair of pre-eruption dimmings, seen in soft X-rays, is in the feet and legs of the quadrupole's central inner lobe with the magnetic arcade straddling the filament. Another pre-eruption dimming, this one in EUV, is apparently in loops of one of the quadrupole's two sidelobes. Parts of both sidelobes gradually brighten in SXT during the slow rise of the filament.

There have been several studies of eruptions involving intensity dimmings using data from *Yohkoh* and *SOHO*, and some of the findings regarding time of occurrence seem to be contradictory: Zarro et al. (1999) found that EUV dimmings occurred virtually concurrent with the onset of flare-associated brightenings; other studies, however, found EUV dimming beginning well before the onset of flare brightenings (Gopalswamy et al. 1999, 2001). Our strongest dimmings are our eruption dimmings, which are similar to those of Zarro et al. (1999) in that they occur very near the eruption region and show a sharp drop in intensity coincident with flare-intensity increase. It is less clear, however, how our pre-eruption dimmings relate to those of Gopalswamy et al. (1999). In their case, the strongest EUV dimming occurred prior to onset of the soft X-ray flare, while our strongest dimming occurs after onset of the soft X-ray flare. Their event was larger than ours, involving disappearance of trans-equatorial structures, and this may be a fundamental difference between the two cases. Thompson et al. (1999) also observed dimmings for a number of eruptions, but their events occurred too rapidly to draw clear

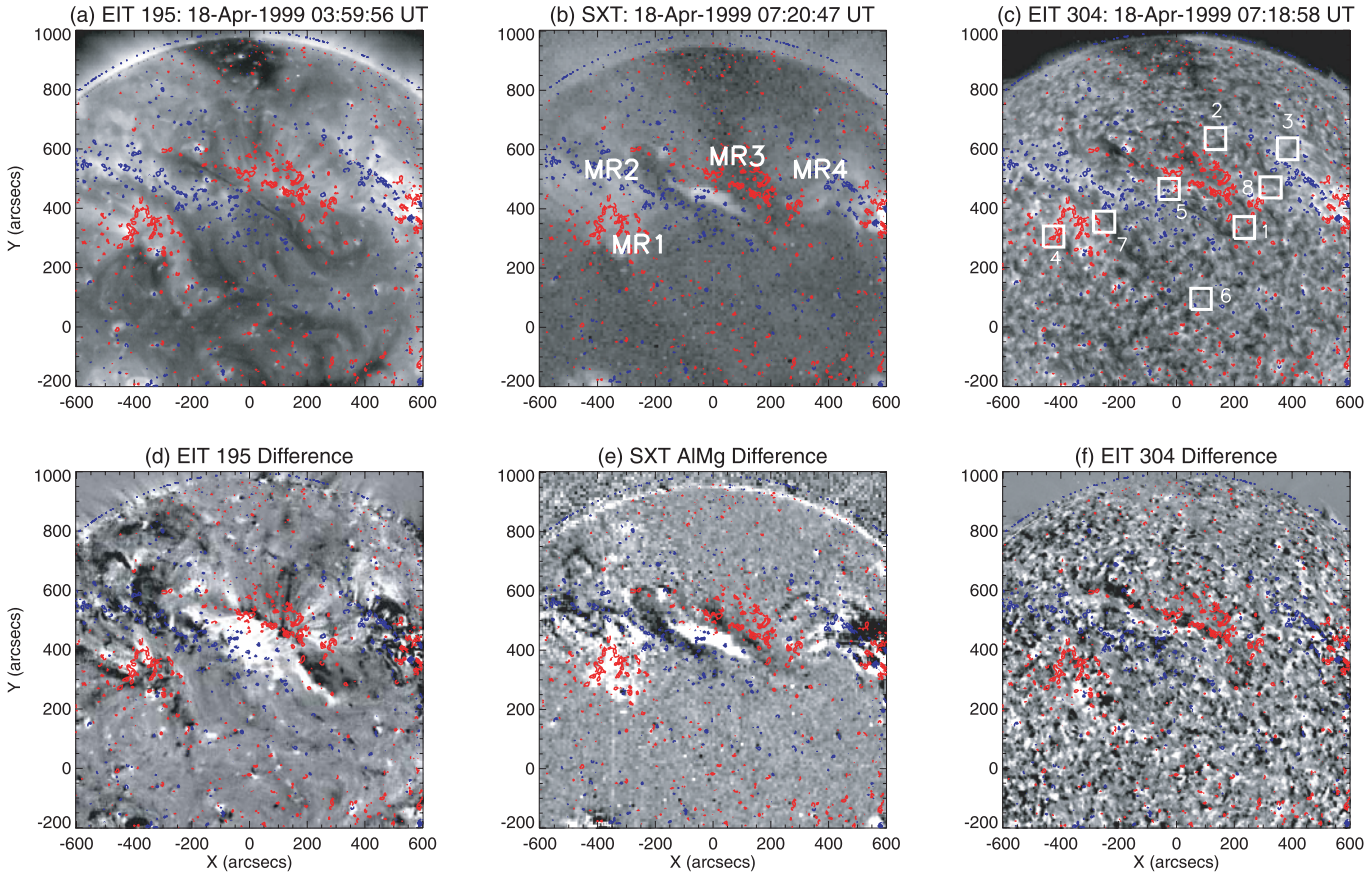

FIG. 8.—Images from (*a*) EIT 195 Å, (*b*) SXT AlMg, and (*c*) EIT 304 Å at the times listed in the respective titles, overlaid with an MDI magnetogram taken at 1999 April 18 04:48:03 UT with red and blue indicating positive and negative polarities, respectively. Annotations in (*b*) give the identifications of the four magnetic regions (MR) of alternating polarities discussed in the text. The filament is visible in (*a*) and (*c*) located between magnetic regions 2 and 3. The bottom row shows the same magnetogram overlaid on difference images in: (*d*) EIT 195 Å with a 1999 April 18 01:35:55 UT image subtracted from the 1999 April 18 10:48:22 UT image in (*a*); (*e*) SXT AlMg with a 1999 April 18 01:34:07 UT image subtracted from the 1999 April 18 07:20:48 UT image in (*b*); and (*f*) EIT 304 Å with a 1999 April 17 19:18:53 UT image subtracted from the 1999 April 18 07:18:59 UT image in (*c*). Boxes in (*c*) identify the same locations as those in Fig. 6.

conclusions about the timing of the dimmings compared to flare brightenings.

In our event, after eruption, the soft X-ray structures appear weakly sigmoid (Sterling & Hudson 1997; Pevtsov 2002; Gibson et al. 2002) with an inverse-S shape (Fig. 2*c*). For active region sigmoid events, the posteruption emission is typically dominated by the postflare loops, and so the sigmoid appearance is lost, but here the eruption is weak enough and of large enough scale so that a sigmoid shape is visible posteruption. In contrast, a sigmoid is not visible in the pre-eruption phase (Fig. 2*a*), probably because of the weakness of the fields. Nonetheless, the magnetic setup is typical of that of sigmoids (cf. Sterling et al. 2000, Fig. 9).

4.1. *Implications for Eruption Mechanisms: Tether Cutting*

As mentioned in § 1, we consider our results in terms of two different eruption mechanisms: tether cutting and breakout. If the transition from the slow phase to the fast phase of the eruption was caused by the onset of runaway tether-cutting reconnection, then we would expect flare brightening to begin in the core field almost simultaneously with the onset of the fast phase (Moore & Roumeliotis 1992; Moore et al. 2001). Since they saw no substantial brightening prior to eruption, Sterling et al. (2001b) concluded that tether-cutting reconnection was not a viable explanation for the eruption onset, unless that reconnection occurred with only low emission measure. Figure 7 shows this also with the filament erupting prior to the major intensity increase of the Figure 6 box 5 light curve. (We have also considered a box that specifically covers the full extent of the core bright feature visible near the center of Fig. 1*e*, using a box covering from $-70''$ to $50''$ in the x-coordinate and $430''$ to $480''$ in the y-coordinate, assuring that we are seeing out to the footpoints of the earliest post-flare loops. The time of EUV intensity increase onset from this box is identical, within our time resolution, to that of the box 5 light curve in Fig. 7.)

We now reconsider this timing question. EIT's cadence is sufficient to say that brightenings in EIT 195 Å do not become large (greater than about 10%) until at least 07:25 UT, which is at least 37 minutes after the start of the rapid filament rise, which occurred between 06:36 UT and 06:48 UT. SXT data, however, have a gap between 06:33 UT and 07:20 UT, and so we do not know when the soft X-ray brightening began relative to the filament's eruption onset. In particular, with this data set, we cannot rule out the possibility that soft X-ray brightenings in the magnetic core were essentially concurrent with the start of the explosive eruption, which is expected from tether cutting (Moore et al. 2001). Therefore the claim of Sterling et al. (2001b) of "first eruption, then reconnection" may have been premature. We can only say with certainly that we see no evidence for reconnection in the X-ray image before the gap; that 06:33 UT SXT image is at least 2 minutes before the start of the explosive phase. The question of the exact timing of tether-cutting reconnection onset relative to the eruption start cannot be answered with this data set.

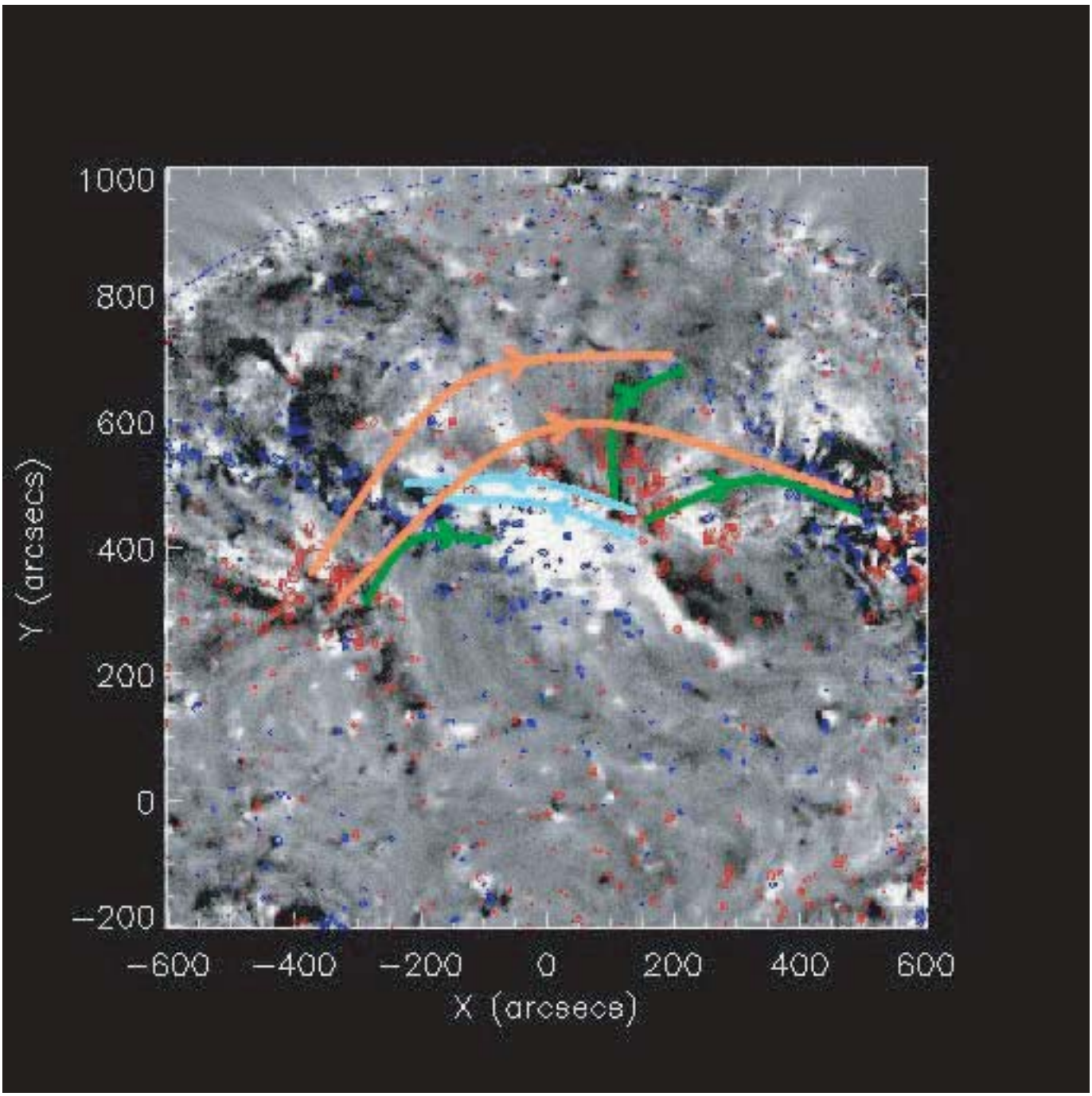

FIG. 9.—Same EIT 195 Å difference image and magnetogram as in Fig. 8*d*, overlaid with curves representing field-line connections that, based on the magnetogram, we expect to exist before the eruption and that we expect to play an active role if the breakout mechanism is responsible for the eruption. These fields are rooted in or near dimming regions, suggesting that dynamic changes occurred in these fields or closely adjacent fields over the time period of the difference image. According to the breakout scenario, before the eruption, the low-lying sheared blue field is restrained by the overlying orange field. Slow upward expansion of the blue field would result from slow reconnection between the blue and orange fields, which would add new heated green-field coronal loops to the sidelobes. After enough of the orange field is removed, the fast eruption starts and much of the erupting blue field escapes as a CME. Reconnection reclosing of the legs of the escaping blue field lines produces the flare arcade and flare ribbons over and along the filament channel.

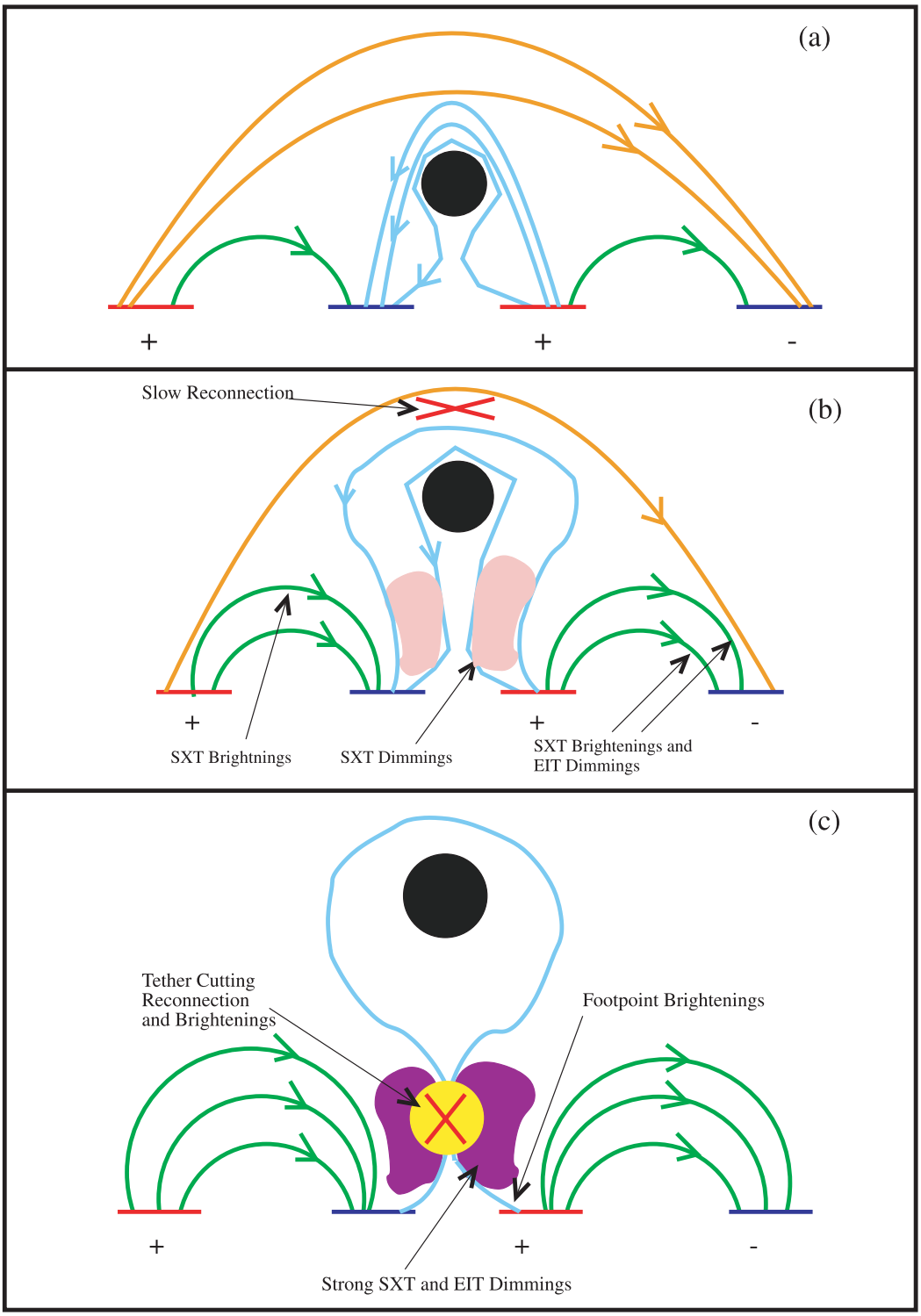

FIG. 10.—Two-dimensional schematic of the observed evolution in the quadrupolar region before and during the explosive phase of the eruption, interpreted as slow breakout leading to the onset of the explosive phase. Onset of the explosive phase is caused either directly by the breakout reconnection itself or indirectly by it rendering a change in the core field that allows the onset of tether-cutting reconnection. (*a*) The situation prior to the slow upward movement. (*b*) During the slow upward movement, the blue field interacts with the overlying orange field via slow breakout reconnection, making new green sidelobe fields; some of these new loops show up as brightenings in SXT and sometimes as dimmings in EIT. SXT dimmings result from expansion of the blue field. (*c*) After enough of the orange field is removed, the remaining blue field in and around the filament explodes out as an erupting filament and CME. Strong dimmings appear in the evacuated legs of the filament-lobe fields that are "opened" by the eruption. Tether-cutting reconnection creates flare ribbons and low-lying flare loops from early on in the explosive phase; we cannot tell whether this reconnection begins concurrent with or just after the onset of the rapid filament ejection.

We also recognize, however, that our expectations for the relation between eruption timing and EUV and soft X-ray brightenings in the tether-cutting concept is only qualitative, as there have been no numerical simulations specifically testing the tether-cutting predictions.

Nevertheless, we do have clear evidence (from Figs. 2*b*, 3*b*, and 8*b*) that the flare loops and ribbons first brightened (and hence tether cutting started) early in the ejection, while the rapidly rising filament was still visible in the EIT Fe XII and He II images. Thus, tether-cutting reconnection was occurring early in the explosive phase and so may have further unleashed the explosion even if it did not initiate the explosion.

4.2. *Implications for Eruption Mechanisms: Breakout*

We now consider whether the breakout mechanism could explain our observations. Breakout requires a multipolar setup, and this certainly exists, as indicated by Figure 8. Figure 9 shows the EIT difference image and magnetogram of Figure 8*d*, on which we have drawn in the field lines that we would expect to play a role if breakout was occurring. We do not actually calculate these fields, some of which are likely to be nonpotential, but instead present our guess for their arrangement based on the magnetograms. The low-lying blue field lines indicate a sheared pre-eruption core field. According to the model, this field pushes upward, because of either flux emergence or further shearing. It would interact with the overlying orange field, driving "slow reconnection" between the blue and orange fields. This reconnection would add new outer loops to the quadrupole's sidelobes, represented by green lines in the figure. When enough of the overlying orange field is removed, the remaining portion of the core blue field would breakout, leading to the eruption and the CME. Reconnection of the outstretched core field lines would result in the flare brightenings and post-flare loops in accord with the standard reconnection flare model.

Our pre-eruption dimmings in EUV north of the eruption region between magnetic regions 3 and 4 and brightenings in soft X-rays between these two magnetic regions occur where one set of the green fields are expected. Similarly, EUV dimmings near magnetic regions 1 and 2 and soft X-ray brightenings between those regions occur where breakout predicts the other set of green field lines to be. Moreover, these dimmings and brightenings began prior to the eruption of the filament, which again is as expected by breakout. The soft X-ray brightenings appear, as best we can tell with the uncertainties in intensity levels, to reach a maximum at the time of the filament's rapid eruption; this agrees with breakout, since the reconnections resulting in new green lobe fields should end once the filament leaves the eruption source vicinity. EUV dimmings in box 2 of Figure 7 show a tendency to follow the filament's evolution, which could indicate heating occurring in these loops, analogous to the soft X-ray brightenings of boxes 7 and 8. Box 3 brightenings are weak in SXT, but they may be similar to those seen in boxes 7 and 8. EUV dimmings in box 4 provide additional evidence for a magnetic connection with the fields involved in the filament eruption. Therefore, our observations in the difference images are generally consistent with predictions of the breakout model.

There still remain, however, uncertainties about whether breakout is actually operating. We do not, for example, see evidence for the pre-eruption overlying fields (the orange field lines in Fig. 9) in the SXT images. Even if our data are showing signatures of breakout-like external reconnections, we have not shown that those external reconnections are essential to the eruption; it is possible that they are instead an indirect response to a different, more fundamental mechanism that actually causes the eruption. Also, if the breakout model is operating during the filament's slow rise in the pre-eruption period, it is still uncertain whether the same mechanism leads to the rapid eruption of the filament. Another possibility is, for example, that the system evolves gradually via the slow breakout reconnection to a state in which runaway tether-cutting reconnection begins in the core field, and that this internal reconnection unleashes the explosive phase of the eruption. Similar observations of different eruptions and complementary numerical studies would help to resolve such outstanding questions.

Figure 10 is an approximate two-dimensional cross section schematic of Figure 9. It summarizes the interpretation of our observations in terms of the breakout and tether-cutting models.

4.3. *Implications for Eruption Mechanisms: Other Ideas*

Other than tether cutting and breakout, we have not considered in detail any of the many other ideas (see, e.g., Forbes 2000) for the onset of solar eruptions; we make no claims as to whether our findings are or are not consistent with such other models. As with the tether-cutting model, many of these do not require a global multipolar setup (e.g., Low & Zhang 2002; Chen 1996; Chen & Shibata 2000; Rust 2001). This in itself, of course, does not make those models inconsistent with our findings here, since any of these largely bipolar mechanisms would be expected to operate in a multipolar environment also. Whether a multipolar setup is essential to eruptions is not clear. In addition to breakout, Uchida et al. (1999) also present a model for eruptions with an intrinsic multipolar character. On the observational side, Manoharan et al. (1996) also present observations of a large-scale eruption that involves multipolar fields. In contrast, Moore et al. (2001) argue that only bipoles dominate in each of the eruptions in their study. It would be of interest to check such suspicions of purely bipolar eruptions with, e.g., dimming patterns in EUV. Moore et al. (2001) could not do such checks, however, since all of their events occurred prior to the launch of *SOHO*.

We thank R. Dean, B. Hargrave, T. Towle, and K. Yoshimura for computer assistance and T. Kosugi for in-residence support in Japan. We also thank G. A. Gary for discussions and D. M. Zarro for much help with the SolarSoft mapping software. Both authors were supported by funding from NASA's Office of Space Science through the Solar Physics Supporting Research and Technology Program and the Sun-Earth Connection Guest Investigator Program. *Yohkoh* is a mission of the Institute of Space and Astronautical Sciences (Japan), with participation from the US and UK and *SOHO* is a project of international cooperation between ESA and NASA.

REFERENCES

Antiochos, S. K. 1998, ApJ, 502, L181
Antiochos, S. K., DeVore, C. R., & Klimchuk, J. A. 1999, ApJ, 510, 485
Chen, J. 1996, J. Geophys. Res., 101, 27499
Chen, P. F., & Shibata, K. 2000, ApJ, 545, 524
Delaboudiniere, J.-P., et al. 1995, Sol. Phys., 162, 291
Forbes, T. G. 1990, J. Geophys. Res., 95, 11919

Forbes, T. G. 2000, J. Geophys. Res., 105, 23153
Gibson, S. E., et al. 2002, ApJ, 574, 1021
Gopalswamy, N., Kaiser, M. L., MacDowall, R. J., Reiner, M. J., Thompson, B. J., & St. Cyr, O. C. 1999, in AIP Conf. Proc. 471, Solar Wind Nine, ed. S. R. Habbal, R. Esser, J. V. Hollweg, & P. A. Isenberg (New York: AIP), 641
Gopalswamy, N., St. Cyr, O. C., Kaiser, M. L., & Yashiro, S. 2001, Sol. Phys., 203, 149
Gopalswamy, N., & Thompson, B. J. 2000, J. Atmos. Terr. Phys., 62, 1457
Harra, L. K., & Sterling, A. C. 2001, ApJ, 561, L215
Hirayama, T. 1974, Sol. Phys., 34, 323
Hudson, H. S., Lemen, J. R., St. Cyr, O. C., Sterling, A. C., & Webb, D. F. 1998, Geophys. Res. Lett., 25, 2481
Innes, D. E., et al. 1999, Sol. Phys., 186, 337
Kahler, S. W., Webb, D. E., & Moore, R. L. 1981, Sol. Phys., 70, 335
Low, B. C., & Zhang, M. 2002, ApJ, 564, L53
Manoharan, P. K., van Driel-Gesztelyi, L., Pick, M., & Demoulin, P. 1996, ApJ, 468, L73
McAllister, A. H., Kurokawa, H., Shibata, K., & Nitta, N. 1996, Sol. Phys., 169, 123
Moore, R. L., & LaBonte, B. 1980, in IAU Symp. 91, Solar and Interplanetary Dynamics, ed. M. Dwyer & E. Tandberg-Hanssen (Dordrecht: Reidel), 207
Moore, R. L., & Roumeliotis, G. 1992, in IAU Colloq. 133, Eruptive Solar Flares, ed. Z. Svestka, B. V. Jackson, & M. E. Machado (Berlin: Springer), 69
Moore, R. L., Sterling, A. C., Hudson, H. S., & Lemen, J. R. 2001, ApJ, 552, 833
Pevtsov, A. A. 2002, Sol. Phys., 207, 111
Rust, D. M. 2001, J. Geophys. Res., 106, 25075
Scherrer, P. H., et al. 1995, Sol. Phys., 162, 129
Schmieder, B., Delannée, C., Yong, D. Y., Vial, J. C., & Madjarska, M. 2000, A&A, 358, 728
Shibata, K., Masuda, K., Shimojo, M., Hara, H., Yokoyama, T., Tsuneta, S., Kosugi, T., & Ogawara, Y. 1995, ApJ, 451, L83
Sterling, A. C., & Hudson, H. S. 1997, ApJ, 491, L55
Sterling, A. C., Hudson, H. S., Thompson, B. J., & Zarro, D. M. 2000, ApJ, 532, 628
Sterling, A. C., & Moore, R. L. 2001a, J. Geophys. Res., 106, 25227
———. 2001b, ApJ, 560, 1045
Sterling, A. C., Moore, R. L., Qiu, J., & Wang, H. 2001a, ApJ, 561, 1116
Sterling, A. C., Moore, R. L., & Thompson, B. J. 2001b, ApJ, 561, L219
Sturrock, P. A. 1989, Sol. Phys., 121, 387
Thompson, B. J. et al. 1999, ApJ, 517, L151
Tsuneta, S., et al. 1991, Sol. Phys., 136, 37
Uchida, Y., Hirose, S., Cable, S., Morita, S., Torii, M., Uemura, S., & Yamaguchi, T. 1999, PASJ, 51, 553
Zarro, D. M., Sterling, A. C., Thompson, B. J., Hudson, H. S., & Nitta, N. 1999, ApJ, 520, L139
Zhang, J., & Wang, J. 2001, ApJ, 554, 474